Data Compression for Close-Range Radar Imaging

Rainer Rückert[ID], Ingrid Ullmann[ID], *Member, IEEE*, Christian Herglotz[ID], *Member, IEEE*,
André Kaup[ID], *Fellow, IEEE*, and Martin Vossiek[ID], *Fellow, IEEE*

Abstract— The resolution of radar images is constantly increasing. As a result, radar images require more storage space, which is associated with increased costs. Therefore, it is advantageous to minimize the data size. In this paper, we present various compression methods for reducing the data size of radar images. Compression and decompression are performed in two scenarios. In the first scenario, the raw data are compressed and decompressed before the image is reconstructed. In the second scenario, the reconstructed image itself is compressed and decompressed. In both scenarios, the reconstructed radar image is compared with the original image. Due to its widespread use, High-Efficiency Video Coding (HEVC) is used as a state-of-the-art benchmark for both scenarios and compared with proprietary algorithms that combine lossy and lossless compression. A discrete Fourier transform–based compression algorithm from the automotive sector is used as another state-of-the-art benchmark. This is applied against our novel approaches, which are based on the discrete cosine transform, use of direct thresholding in the spatial domain, or are applied to the maximum intensity projection. With the exception of HEVC, all algorithms presented have in common that they perform lossy data processing in the first step and then use the Lempel–Ziv–Markov algorithm as a lossless compression step. To compare the compression ratios, we use various image- and video-specific metrics, such as the peak signal–to-noise ratio (PSNR), the similarity of speeded-up robust features, and the structural similarity index measure (SSIM). For a simple classification, we use Otsu's method to examine the effects of compression on the images. The radar images are categorized into transparent and nontransparent based on the measurement objects. Depending on the application and the desired resolution, our approaches can achieve storage savings of up to 99.93 % compared to the uncompressed data with PSNR and SSIM values of 38.8 dB and 0.916, respectively.

Index Terms— Compression, data, discrete cosine transform (DCT), discrete Fourier transform (DFT), high-efficiency video coding (HEVC), imaging, peak signal-to-noise ratio (PSNR), radar, structural similarity index measure (SSIM), speeded-up robust features (SURF), thresholding.

I. INTRODUCTION

IN recent years, close-range radar imaging has been increasingly used in various applications, such as security screening [1], nondestructive testing [2], and autonomous driving [3]. In all these areas, artificial intelligence is incorporated into further processing to automatically detect objects in security screening or material defects in nondestructive testing, and it will undoubtedly be indispensable for autonomous driving.

To achieve good classification results using machine learning, large datasets are needed to train networks. Consequently, large amounts of data must be obtained and stored. To reduce the required storage, data compression techniques will attract increasing interest as machine learning is used in a growing number of applications.

Whereas data compression has been widely studied in image processing, and standards for 1D [4], 2D [5], and 3D [6] space data have been defined by the Consultative Committee for Space Data Systems, few such attempts have been made specifically for radar imaging. Some work has been conducted in the context of surveillance [7] and remote sensing with synthetic aperture radar (SAR) [8], [9], [10] or inverse SAR (ISAR) [11]. However, as demonstrated, for example, in [12], close-range radar data which we target in this paper, are different from typical remote sensing data. For close-range applications, only one study has been conducted [13]. This study aimed to compress automotive radar data, which are often sparse by nature and makes compression straightforward. With high-resolution radar images, the situation is different. Such images are often similar to optical grayscale images. An illustration of a 3D radar cube with the corresponding dimensions is shown in Fig. 1 [14].

Principally data compression techniques can be adapted from image processing. However, radar images differ from photographs in some points: First, they are generated from raw radar measurement data by reconstruction algorithms [15], [16]. Therefore, unlike optical images, both the radar image and the raw measurement data are candidates for compression. Second, radar data are generally three-dimensional and provide depth information in addition to two-dimensional image information. Due to their 3D shape, radar images are also referred to as image volumes. Third, radar image data are typically complex valued, as they contain amplitude and phase information.

For these reasons, we aim to explore new approaches for close-range radar image compression. The core contributions of this work are the use of existing compression algorithms,
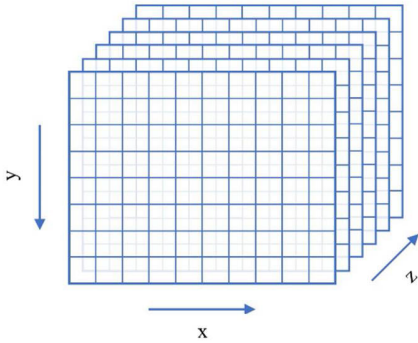
Fig. 1. Illustration of a radar cube for close-range radar imaging [14].

such as High-Efficiency Video Coding (HEVC) and the discrete Fourier transform (DFT)-based algorithm used in [13] for automotive applications, and their comparison with new compression algorithms presented here.

The rest of this paper is organized as follows: Section II describes the measurement setup and the transparent and nontransparent test objects used in this study. Section III introduces the metrics used for the evaluation of data compression. Section IV presents the algorithms used for data compression. Section V presents the compression performance of the algorithms on raw and reconstructed image data. Section VI details the effects of the algorithms on the compressed radar images. Section VII concludes the paper.

II. MEASUREMENT SETUP AND TEST OBJECTS

To apply data compression to radar images, we performed measurements using a network analyzer–based synthetic aperture radar test bench available at our institute (Fig. 2). An overview of the measurement setup is provided in Table I. More details can be found in [17]. We used stepper motors to move the antennas along a predefined trajectory. The measurement points are scanned line by line, progressing from left to right in one line and from right to left in the subsequent line. There is no movement of the antennas during the measurement. The dimensions of the resulting raw data are influenced by the number of measurement points in both the x and y directions as well as the frequency steps N_f, represented in the format $y \times x \times N_f$.

We investigated two scenarios: one with a test object that was transparent to the radar waves and one with a nontransparent object. As a transparent object, we used a closed cardboard box of $300 \times 250 \times 80$ mm^3 with potential threat objects inside it as seen in Fig. 3 resulting in raw data dimensions $311 \times 351 \times 201$. To better quantify the resolution, we also placed a Siemens star in the box. The tips of the star converged radially in the middle. The finer the central dot, the better the resolution, which is determined by the center's diameter.

As a nontransparent object, we adopted a case from medical radar imaging: we used a 3D-printed metallized hand to simulate a human hand with raw data dimensions $351 \times 201 \times 201$. Human hand imaging is relevant to gesture sensing and medical diagnoses—for example, in the detection of arthritis [18]. For millimeter waves, the human skin acts like
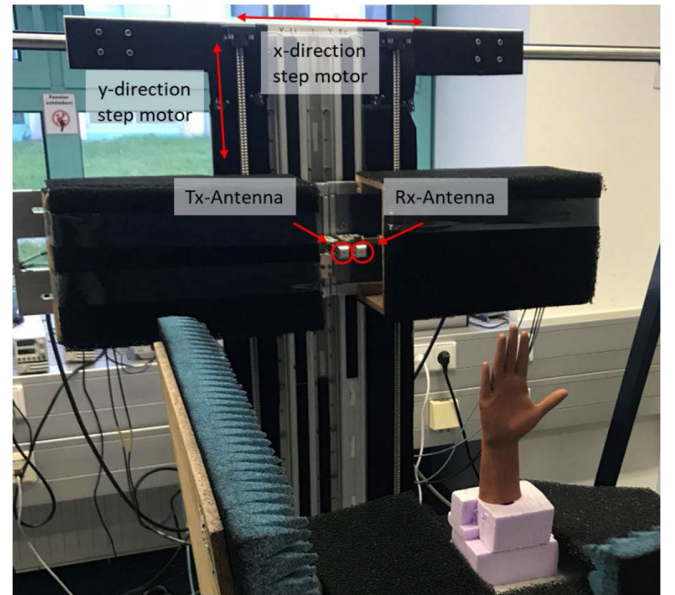

Fig. 2. Photograph of the 3D-printed metallized hand used as a nontransparent test object in front of the radar test bench.

TABLE I
OVERVIEW OF THE MEASUREMENT SETUP

Vector network analyzer	Rohde & Schwarz ZVA 24
Extenders	Rohde & Schwarz ZVA-Z110
Signal form	Stepped-Frequency Continuous-wave
Number of frequency steps	201
Frequency range	75–110 GHz
Antennas	2 linearly polarized horn antennas
Antenna configuration	Quasi-monostatic
Antenna trajectory	350×310 mm² and 200×350 mm² with 1 mm step width in the x and y directions

a perfect reflector due to its substantial water content. Thus, radar beams are completely reflected on the skin's surface and cannot penetrate into deeper structures. A metallized object is well suited for simulating this behavior since metal completely reflects the radar waves as well. Fig. 2 shows the measurement setup with the test object.

The cross-range resolution $\delta_{x,y}$ for the x or y direction, can be calculated as

$$\delta_{x,y} \approx \frac{\lambda}{D_{x,y}} \cdot L \tag{1}$$

where λ denotes the wavelength, $D_{x,y}$ represents the aperture length in the x or y direction and L the distance between aperture and object [16]. In our case, the box was placed between 260 mm and 355 mm from the aperture, while the hand was positioned between 320 mm and 355 mm away. This yields mean values for the cross-range resolution of 3 mm and 4.24 mm, respectively. The resolution in z direction is determined by

$$\delta_z \approx \frac{c_0}{2 \cdot B} \tag{2}$$

Fig. 4. Layers 78 and 84 of the box image with a distance of 6 mm in the z direction. With increasing viewing depth, the pack of powder and the knife disappeared, while the Siemens star and the scissors could be seen more clearly. The bottle was not visible because it lay in layers 52–70.

Fig. 5. Images of the hand (a) and the maximum intensity projection (b).

it is important to note that the normalization process comes with the drawback of losing absolute amplitude information. Fig. 4 shows layers 78 and 84 of the 96 layers of the resulting image volume for the box, with a distance of 6 mm along the depth direction (herein denoted by z).

The total sizes of the raw data are 175.53 MB and 113.45 MB for the box and hand images, respectively. The corresponding sizes of the image volumes are 83.835 MB and 54.183 MB. This is due to the reconstruction algorithm converting the 201 frequency steps into 96 depth layers.

To visualize a 3D volume in two dimensions, the maximum intensity projection [18] is often used. This method extracts the pixel with the maximum image intensity along the depth direction for every lateral image point (x, y). Fig. 3(c) and Fig. 5(b) show the maximum projections for the test objects as grayscale images. The brighter an object appears, the higher the amplitudes of the reflected radar waves.

III. DATA COMPRESSION METRICS

To compare the reference image I with the compressed image J and evaluate the data compression performance, we used various metrics, which are described below.

A. Peak Signal–to-Noise Ratio

The peak signal–to-noise ratio (PSNR) is an established metric for image comparisons [22]. Referring to the maximum amplitude A of the image, the PSNR is calculated as

$$\text{PSNR}_{\text{image}} = 10\text{dB}\cdot\log_{10}\left(\frac{A^2}{\sigma_{\text{e}}^2}\right) \tag{4}$$
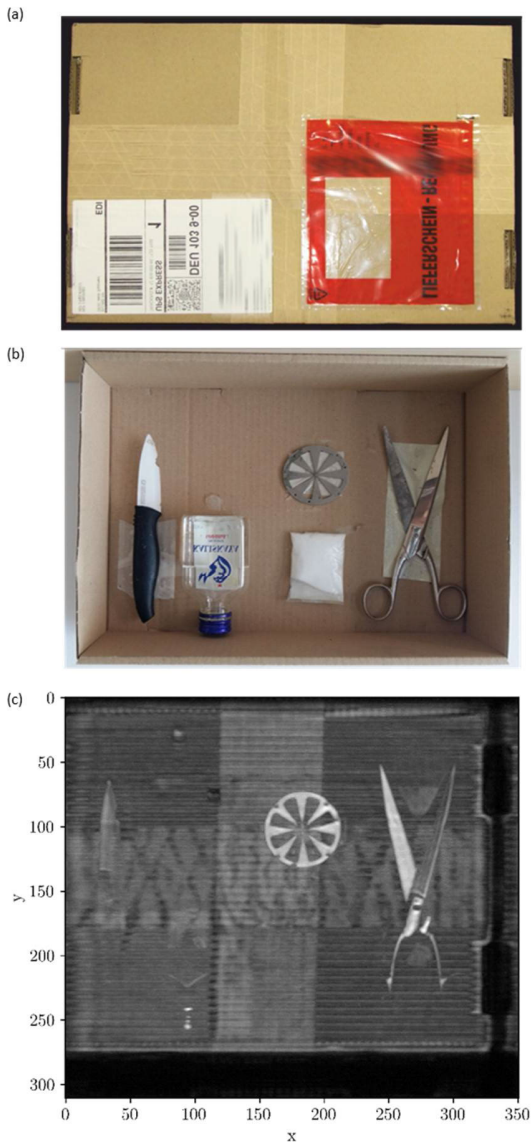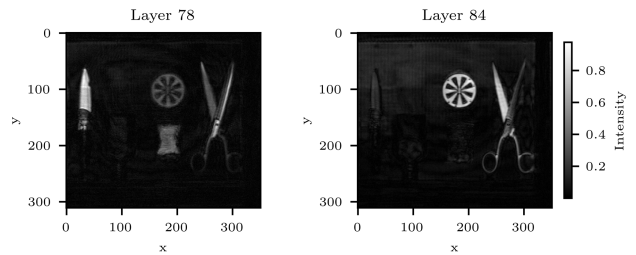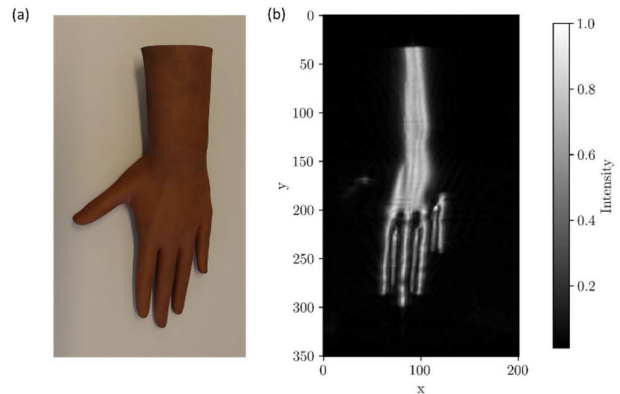

Fig. 3. (a) The outside of the box, (b) the inside of the box (b), and (c) the resulting maximum intensity projection of the closed box with the packing tape to seal the box. The box contained a knife, a bottle filled with a liquid, a pack of powder, a pair of scissors, and a Siemens star for resolution comparison.

where c_0 represents the velocity of light and B the bandwidth [16]. With $B = 35$ GHz (see Tab. I), the resolution in z direction for the box and hand image results in 4.3 mm. The unambiguous range in the z direction z_{A} is calculated as [19]

$$z_{\text{A}} = \frac{c_0 \cdot (N_f - 1)}{2 \cdot B} \tag{3}$$

which results in 857 mm for both.

To obtain a radar image from the measurement data, an image reconstruction algorithm must be used. In this work, we used the phase-shift migration method, as described, for example, in [20] and [21]. The algorithm reconstructs a 3D image volume. Given that, in most applications, amplitudes are normalized to the range [0, 1], and the phase information is not further utilized, this paper also adopts this approach. However,

with variance, also known as mean square error,

$$\sigma_e^2 = E\big((I(x, y) - J(x, y))^2\big) \qquad (5)$$

between I and J, with E denoting the expected value and x and y denoting width and height coordinates of the image, respectively.

For measurements involving nontransparent objects, (4) is applied to the maximum intensity projection. For measurements involving transparent objects, the comparison is performed on the 3D image volume. In this case, (4) is changed to

$$\text{PSNR}_{\text{video}} = 10 \text{ dB} \cdot \log_{10}\left(\frac{A^2}{\frac{1}{K} \cdot \sum_{k=0}^{K-1} \sigma_e^2[k]}\right), \qquad (6)$$

where K is the number of images in a sequence—in this case, the number of depths. In this study, all amplitudes were linearly normalized to 1 as a basis and resulting in $A = 1.0$.

B. Speeded-Up Robust Features

To detect similar regions in two images, machine learning algorithms perform feature extraction. A widely used algorithm is the speeded-up robust features (SURF) [23], which detects edges and corners in images and their geometric properties. Based on the internal statistics, the SURF algorithm produces a vector that includes the coordinates of the pixels by searching for visually interesting features in an image. Similar regions can be indicated by comparing the extracted features between images I and J. If the coordinates of the features in images I and J are the same, a match is found [13].

The SURF recall value is calculated as

$$\text{SURFrecall}(I, J) = \frac{matchedFeat(I, J)}{detectedFeat(I)} \qquad (7)$$

where $matchedFeat$ represents the number of matched features in I and J, and $detectedFeat$ represents the number of detected features in I. This value indicates how well the optical features were preserved after compression and decompression.

As is typical in radar, side lobes occur in addition to the main lobes. When applying the SURF algorithm to nontransparent objects, the side lobes do not pose a problem since they have been truncated in z direction, and the maximum projection is solely focused on the main lobe. However, for transparent objects, the side lobes can overlap with the main lobes of other reflections and, as a result, cannot be separated. Consequently, the side lobes are carried along during the compression process.

C. Human Perception–Based Metric

The structural similarity index measure (SSIM) [22] is used to compare an image I to an image J and calculate the difference. The SSIM is calculated as

$$\text{SSIM}(I, J) = \frac{(2\mu_I\mu_J + c_1)(2\sigma_{IJ} + c_2)}{\big(\mu_I^2 + \mu_J^2 + c_1\big)\big(\sigma_I^2 + \sigma_J^2 + c_2\big)}, \qquad (8)$$

with the variance σ_I, σ_J and the average μ_I, μ_J of I and J, respectively. The covariance of the images is expressed as σ_{IJ}. The division is stabilized using the constants c_1 and c_2 [13].
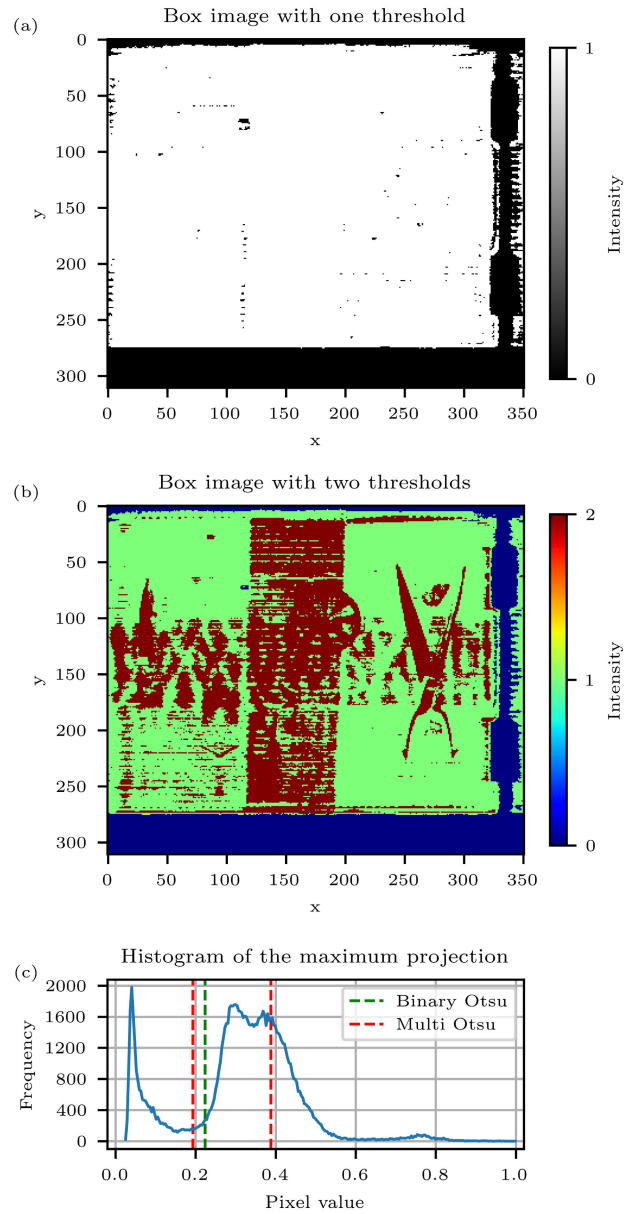

Fig. 6. Comparison between separation into two classes (a) and three classes (b) using Otsu's method. When the maximum projection was separated into two classes, no contents of the box were visible. When it was separated into three classes, some of the items inside the box were visible. In the histogram (c), different thresholds for the two methods are shown.

For measurements involving nontransparent objects, (8) is applied to the maximum projection. For measurements involving transparent objects, the SSIM is calculated based on the 3D image volume [24].

D. Image Segmentation

Because radar images are grayscale images, we used Otsu's method [25] on the maximum intensity projection for a simple classification of images I and J. The algorithm separates an image into two classes, background and foreground, according to a threshold. Pixels with values smaller than the threshold are represented as background (black), whereas the other pixels are represented as foreground (white), as shown in Fig. 6(a). The threshold is calculated using an image histogram [25], [26].

TABLE II
MAJOR PROPERTIES OF THE DIFFERENT ALGORITHMS

HEVC [27]–[29]	+	Frequently used due to available implementation
	+	Uses the dependencies of individual layers
	−	Compression and decompression take a long time due to motion compensation
DFT [13]	+	Considerably faster than HEVC
	+	Execution on the 3D image volume
	+	Noise clipping because the image is transformed into the spatial frequency domain
	−	Due to complex values after transformation, separation into linear amplitude and phase is necessary
	−	Inverse transformation required
DCT	+	Considerably faster than HEVC
	+	Execution on the 3D image volume
	+	Noise clipping because the image is transformed into the spatial frequency domain
	+	No separation into amplitude and phase required
	−	Inverse transformation required
Thresholding	+	Considerably faster than HEVC
	+	Execution on the 3D image volume
	+	Can be performed directly in the spatial domain
	+	No inverse transformation required
MaxCube	+	The fastest algorithm
	+	Good compression ratio with little effort
	−	Execution on the 2D maximum intensity projection
	−	Can be used only on nontransparent measurement objects

If the image is divided into two classes, the contents of the box would be assigned to the foreground and would no longer be recognizable. For this reason, we used the multi-Otsu method with two thresholds. An example of the classification is shown in Fig. 6(b), with blue indicating the background, red indicating the foreground, and green indicating the area between the foreground and background.

IV. DATA COMPRESSION ALGORITHMS

An overview of the algorithms used in this study is provided in Table II. The algorithms are described in detail below.

A. HEVC Video Compression Algorithm

Because a 3D image volume is composed of consecutive images, video coding is suitable for compression. For redundancy reduction, video compression takes advantage of three dimensions: two spatial and one temporal. Further advanced prediction tools use similar content in different frames. One example is motion compensation, which predicts the content of the current frame $I(x, y, z_i)$ based on the content of a previously coded frame $J(x, y, z_i - 1)$. Another benefit is the block-based partitioning scheme, which enables an efficient representation of large areas in images to enhance compression performance [13].

The first compression tool that we used was the HEVC codec [27]. Because radar images are very similar to each other along the depth direction, we used the z direction

(depth) as the temporal dimension (see Fig. 4). As a result, the movement of objects between the pictures, representing a displacement over time in the classical HEVC, is analogously interpreted as a displacement along the z direction in our approach. To encode the sequence, we used the HM-16.22 [28] encoder implementation of HEVC. The configuration of the encoder was random-access encoding [29], in which the coding order of frames differs from the display order. For instance, a five-frame sequence is hierarchically coded in the order of $0 \rightarrow 4 \rightarrow 2 \rightarrow 1 \rightarrow 3$. This method achieves significant bitrate savings because intermediate frames (1, 2, and 3) can be predicted more accurately using both previous and subsequent frames. We applied this scheme to a group of 16 frames. We set the color format to 4:0:0 and used a bit depth of 16 bits per sample with manually quantized input data [13].

B. Discrete Fourier Transform-Based Compression Algorithm

A Discrete Fourier Transformation (DFT)-based compression method was introduced in [13] based on the assumption that it was possible to separate and extract features because of the correlation gain achieved by the DFT. A threshold for an estimated noise floor led to the removal of low values by setting them to zero if they were below the threshold.

Since radar signals have a broad dynamic range, the DFT-transformed values were logarithmically quantized in [13]. In our case, the value range lies in the interval [0, 1] (see Fig. 6(c)). For this reason, we used a linear representation of the values, which resulted in several modifications to the compression method introduced in [13]. The five steps for the encoder were as follows:

1) transforming via an n-dimensional real-valued DFT by discarding negative frequencies;
2) switching to a representation with phase and linear amplitudes;
3) removing the noise floor by setting values below a predefined amplitude threshold to zero;
4) quantizing the resulting values;
5) lossless entropy coding using the Lempel–Ziv–Markov–algorithm (LZMA) [30].

For decoding, these steps are performed in reverse order. It has been investigated whether value quantization should be performed with a logarithmic amplitude and linear phase or with linear real and imaginary numbers. In this study, the best results were achieved using a linear amplitude and phase.

C. Discrete Cosine Transform–Based Compression Algorithm

The discrete cosine transform (DCT), introduced in [31], is widely used for data compression, including image compression (such as JPEG). Our initial approach involves utilizing the DCT, which, like the DFT, transforms a time-discrete signal into the frequency domain. However, unlike the DFT, which produces complex values after transformation, the coefficients obtained by the DCT are real numbers.

The DCT-based algorithm follows the same steps as the DFT for the encoder:

1) transforming via an n-dimensional DCT;
2) removing the noise floor by setting values below a predefined amplitude threshold to zero;
3) quantizing the resulting values;
4) lossless entropy coding using the LZMA.

The decoder follows these steps in reverse using the inverse DCT. The basic process of thresholding and quantization corresponds to the algorithm presented in Section IV-B.

We also tested whether a logarithmic representation of the amplitudes would produce better results. Because the phases of the DFT include the sign of the amplitude and the DCT produces only real coefficients with positive and negative signs, we implemented a method in which the absolute values were logarithmized after the DCT and the sign of the uncompressed values was attached to the absolute values. However, a representation with linear amplitudes showed the best compression ratio.

D. Thresholding Compression Algorithm

The algorithms described in Sections IV-B and IV-C are executed in the spatial frequency domain, which necessitates an inverse transform at the end of the decoding. Our new approach, which we call Thresholding, is to perform the compression directly in the spatial domain of the 3D image $\boldsymbol{I}$. This method does not require the first two steps of DFT compression. For determining the threshold value, one option is Constant False Alarm Rate (CFAR) [32], which estimates noise in a specific area to detect individual targets. Unlike in automotive applications, where only a few targets may surpass the noise, radar imaging typically involves a larger number of targets. When it is used on larger areas containing signal components (see the shear blade in Fig. 3(c)), a higher noise amplitude is typically present in these regions, leading to the subsequent identification of individual point targets within them. If only the areas with detected targets were considered for compression, while the remaining areas were set to zero, a significant portion of the image information would be lost. Hence, the application of CFAR is deemed unsuitable, and instead, a fixed threshold is employed. Thus, process for the encoder is reduced to the following three steps:

1) removing the noise floor by setting values below a predefined amplitude threshold to zero;
2) quantizing the resulting values;
3) lossless entropy coding using the LZMA

Again, the decoder follows these steps in reverse. We also tested a logarithmic representation of the amplitudes, which showed a lower compression ratio.

E. Maximum Cube for Nontransparent Objects

For nontransparent objects, such as the human hand, the fact that radar beams are completely reflected on the surface and do not penetrate into deeper layers can be exploited. Principally nonzero values occur in the deeper layers of the actual measurement object, they are side lobes or noise. So there is only one reflection along the z direction and the maximum projection contains all relevant reflections from the image volume.

Our new approach is to reduce the data by generating two matrices from the image volume. Matrix 1 is the maximum intensity projection, and Matrix 2 contains the index in the z direction in which the respective maximum value in Matrix 1 appears. In a simple way, with no quantizing or changing the data type from float to integer with a lower resolution, the reduction can be performed as

$$\text{ratio} = \frac{n}{2}, \tag{9}$$

where n is the number of depth layers in image $\boldsymbol{I}$. Since only the surface on which the radar waves are reflected is displayed when the two matrices are reconstructed into the 3D image, we call this method the maximum cube (MaxCube).

To obtain a higher compression ratio, we quantize both matrices. While we change the quantization of Matrix 1, to vary the ratio, we quantize Matrix 2 with a fixed number of bits. Due to the 96 layers, we quantize Matrix 2 with 8 bits to signed integer because of the interval of $[-128, 127]$. Again, linear amplitudes for Matrix 1 showed better results than logarithmic amplitudes.

V. Compression Results

We applied all algorithms to the 3D image volumes of the hand and the box. Except for MaxCube, we also applied all algorithms to the raw data. Because the raw data are complex valued, we first separated them into real and imaginary numbers, except in the case of the DFT, which transformed the raw data without discarding the negative frequencies, making the separation into real and imaginary numbers unnecessary. We then ran each algorithm twice to compress the data: once for the real numbers and once for the imaginary numbers. After decompression, we merged the numbers to reconstruct the raw data and generate the image volumes to be compared with the uncompressed images.

Different compression ratios were achieved with different values for the following:
- the quantization parameter for HEVC;
- the threshold and quantization for the DFT- and DCT-based compression algorithms and the Thresholding algorithm;
- the quantization of the maximum intensity projection (Matrix 1) of MaxCube.

The compression ratio was calculated as

$$\text{compression ratio} = \frac{sizeOrig}{sizeComp}, \tag{10}$$

where $sizeOrig$ is the data size of the uncompressed image or the uncompressed raw data, and $sizeComp$ is the size of the reconstructed radar image or the raw data after compression.

A prevalent phenomenon in radar imaging is speckle, which is characterized by multiplicative overlays of radar wave amplitudes. The algorithms described in Sections IV-B and IV-E, incorporating a threshold, significantly mitigate the impact of speckle, making them a valuable addition [33].
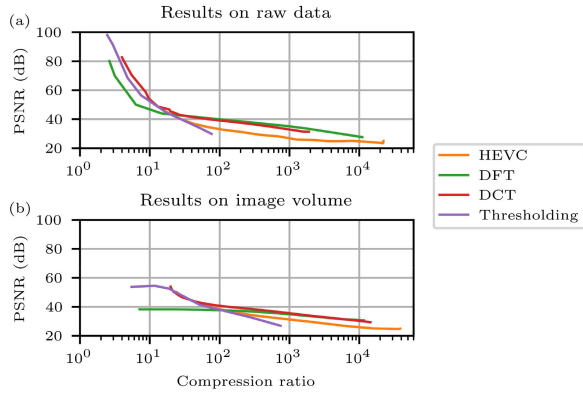
Fig. 7. PSNRs of the box image. (a) raw data and (b) image volume compression results. All four algorithms showed the same tendency. The DFT and DCT performed better than HEVC with higher compression ratios, and Thresholding performed better than HEVC with lower ratios in both raw data and image volume compression.
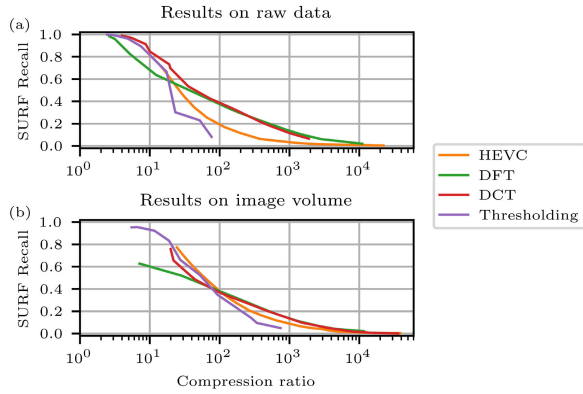

Fig. 8. SURF Recall values of the box image. (a) raw data and (b) image volume compression results. More matches were found when the raw data were compressed. The DCT showed the best raw data compression performance. In image volume compression, HEVC showed the best performance with ratios of up to approximately 100, above which the DFT and DCT performed better.
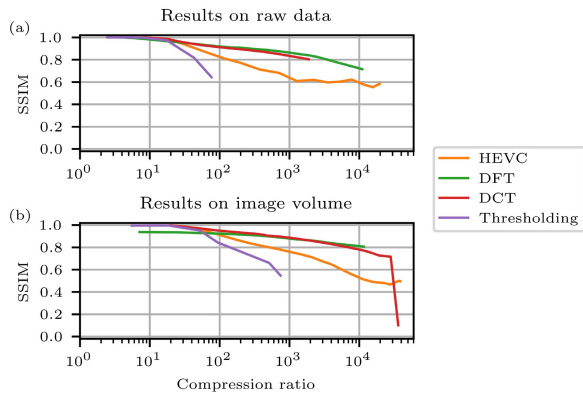

Fig. 9. SSIMs of the box image. (a) raw data and (b) image volume compression results. The DFT and the DCT showed similar raw data compression behavior and performed better than HEVC. In image volume compression, the DCT produced better results than the DFT.

A. Compression of the Box Radar Image

Because the box image volume contained transparent objects, we examined it three-dimensionally. First, we observed the PSNR. Fig. 7 shows the impact of each
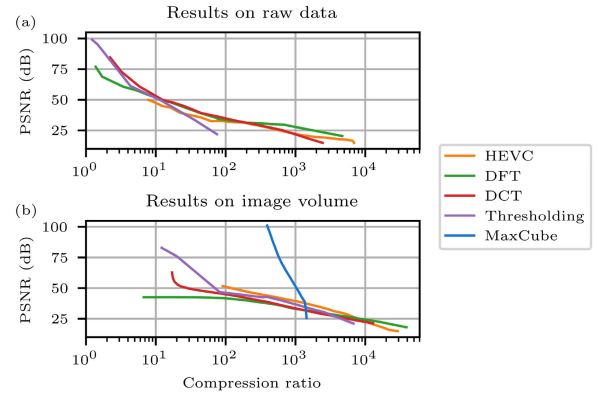

Fig. 10. PSNRs of the hand image. (a) raw data and (b) image volume compression results. Thresholding produced the best results in (a) and (b) with low compression ratios. The DFT and DCT showed similar behavior, but the DCT was better with lower ratios, while the DFT was better with higher ratios. In (b), MaxCube showed the best performance with ratios of up to approximately 1300, above which HEVC showed comparable performance.
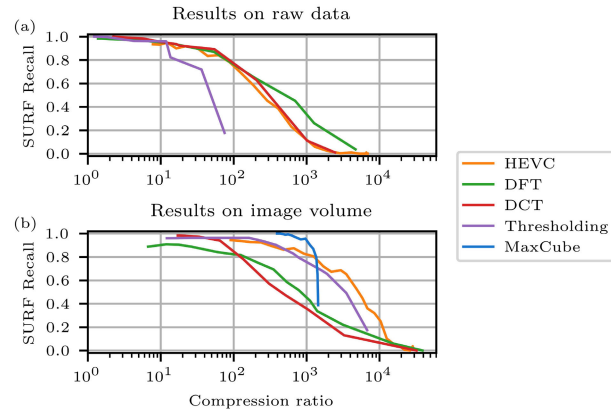

Fig. 11. SURF Recall values of the hand image. (a) raw data and (b) image volume compression results. The DFT produced the best compression results in (a). In (b), Thresholding showed the best performance with lower compression ratios, whereas HEVC showed the best performance with higher ratios. MaxCube performed better than HEVC only with ratios of up to 1300.
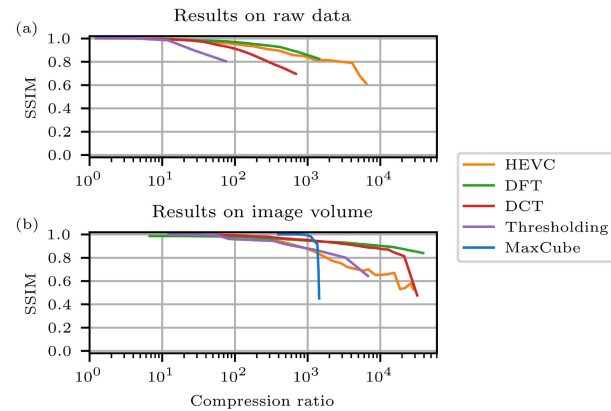
Fig. 12. SSIMs of the hand image. (a) raw data and (b) image volume compression results. The DFT delivered the best raw data and image volume compression results, although in image volume compression, MaxCube performed better with compression ratios of up to 1300.

compression algorithm applied to the raw data (a) and the reconstructed radar image (b). Here, (6) was applied to the image volume, since it contained both transparent and non-

transparent objects. Raw data compression resulted in higher PSNR values. Only for ratios of 10 or higher did the compression of the image volume obtain better results. As a video compression algorithm, HEVC is suitable for compressing 3D data. Nevertheless, the DFT and DCT showed better image volume compression performance. Thresholding was better only with low compression ratios.

We then examined the SURF recall (Fig. 8). All image layers were compared before and after compression, a search for matches was performed, and (7) was calculated for each layer of the image volume. The mean value of the layers was then calculated for the compression. As in the case of the PSNR, when the image volume was compressed (b), higher compression ratios were achieved with higher SURF Recall values. Thus, with compression ratios of 10 or higher, compressing the image volume was more advantageous. Thresholding showed the best performance with ratios of up to approximately 100. With higher ratios, the DFT and DCT performed better than HEVC. In raw data compression (a), the DCT achieved the best results.

Finally, we evaluated the similarity between the images using the SSIM (Fig. 9). While the DCT and DFT followed a similar course when compressing the raw data (a), the graphs diverged when the image volume (b) was compressed in low ratios. The DCT reached a value of 100 %, while the DFT reached a maximum of 94 %. With higher ratios, the DFT and DCT again showed better results than HEVC.

B. Compression of the Hand Radar Image

Since the hand was opaque to radar waves, we examined it two-dimensionally on the maximum intensity projection. First, we observed the PSNR, calculated using (4). As shown in Fig. 10, up to a ratio of 10, higher PSNR values were achieved by compressing the raw data (a). The performance of each algorithm depended on whether the raw data or the image volume was compressed and on the compression ratio. In image volume compression (b), Thresholding showed the best performance when a moderate compression ratio up to 100 was sufficient. With higher ratios, HEVC achieved a higher PSNR. However, MaxCube achieved the best results, even with compression ratios of over 500. Only with compression ratios of 1300 or higher did HEVC outperform MaxCube. In raw data compression (a), the DFT and DCT showed similar behavior with compression ratios of 10–100. With higher ratios, the DCT obtained a lower PSNR than the DFT.

The SURF Recall of the hand image is shown in Fig. 11. Up to 100 % of the initial matches were still found. In raw data compression (a), the DCT and DFT showed the best performance with compression ratios of up to approximately 200. With higher ratios, the DFT performed better. In compressing the reconstructed image volume (b), Thresholding showed the best performance with ratios of up to approximately 500 but was outperformed by HEVC with higher ratios. MaxCube achieved considerably higher SURF Recall values with compression ratios of up to 1300.

As shown in Fig. 12 for the evaluation of SSIM, in image volume compression (b), MaxCube achieved the best results with compression ratios of up to 1300. With higher ratios, the

DFT showed better performance than the DCT and MaxCube. In raw data compression (a), the DFT achieved the best results with compression ratios of up to approximately 1200, above which HEVC performed better.

VI. EVALUATION

To examine the effects of the algorithms, we used the amplitude histograms of the image volumes. Since there were hardly any differences in the histograms before and after the compression of the raw data, they are not reported here. Due to the lack of transparency, the histograms of the hand image showed only one large peak. Therefore, only the evaluation of MaxCube compression is reported. Since the radar waves were reflected by the skin surface in the hand image, and a large area was therefore not radiated, this resulted in many values close to zero. In contrast, the box histograms showed courses with several peaks across the pixel values because the different objects in the image reflected the radar beams at different amplitudes. Thus, we examined the effects of the compression algorithms on the box image more closely.

Since the maximum intensity projection is, in most cases, viewed by humans, and therefore subjective perception is more important than the PSNR or SURF Recall, the SSIM is used to compare various algorithms. In [34], it was shown that a value between 80 % and 100 % was suitable. For comparison, we used the same SSIM value of around 90% for all reconstructed radar images.

A. Box Radar Image Compression Results

For comparison, Fig. 13(a)–(c) shows the box image before compression. The thresholds of Otsu's method, were 0.193 and 0.388.

The HEVC compression results are shown in Fig. 13(d)–(f). Despite a compression ratio of 120 and a resulting data size of 682.2 kB, there were hardly any differences in either the grayscale image or the classification image. The Siemens star was still visible under the adhesive tape at the top of the box, and its center was not enlarged. Otsu's thresholds were 0.185 and 0.383. The histogram in Fig. 13(f) shows that the number of zero values more than doubled. This is because the image volume also contained noise, which represents a high frequency. Since high-frequency components are not transmitted, they are set to zero before transmission.

The DFT compression results, with a compression ratio of 520, a data size of 160.7 kB and Otsu's thresholds of 0.209 and 0.418, are shown in Fig. 13(g)–(i). Some details, such as the glass body of the bottle, were barely recognizable in the grayscale image after compression. Moreover, the edges of the objects were no longer sharp, and the image was blurry. The classification showed, for example, that the green space in the adhesive tape became smaller because Otsu's threshold for the foreground became lower, thus including more values. The spaces in the Siemens star under the adhesive tape also became smaller, and its center expanded significantly. After compression, the maximum value was no longer 1, leading to normalization in the range of [0, 1].
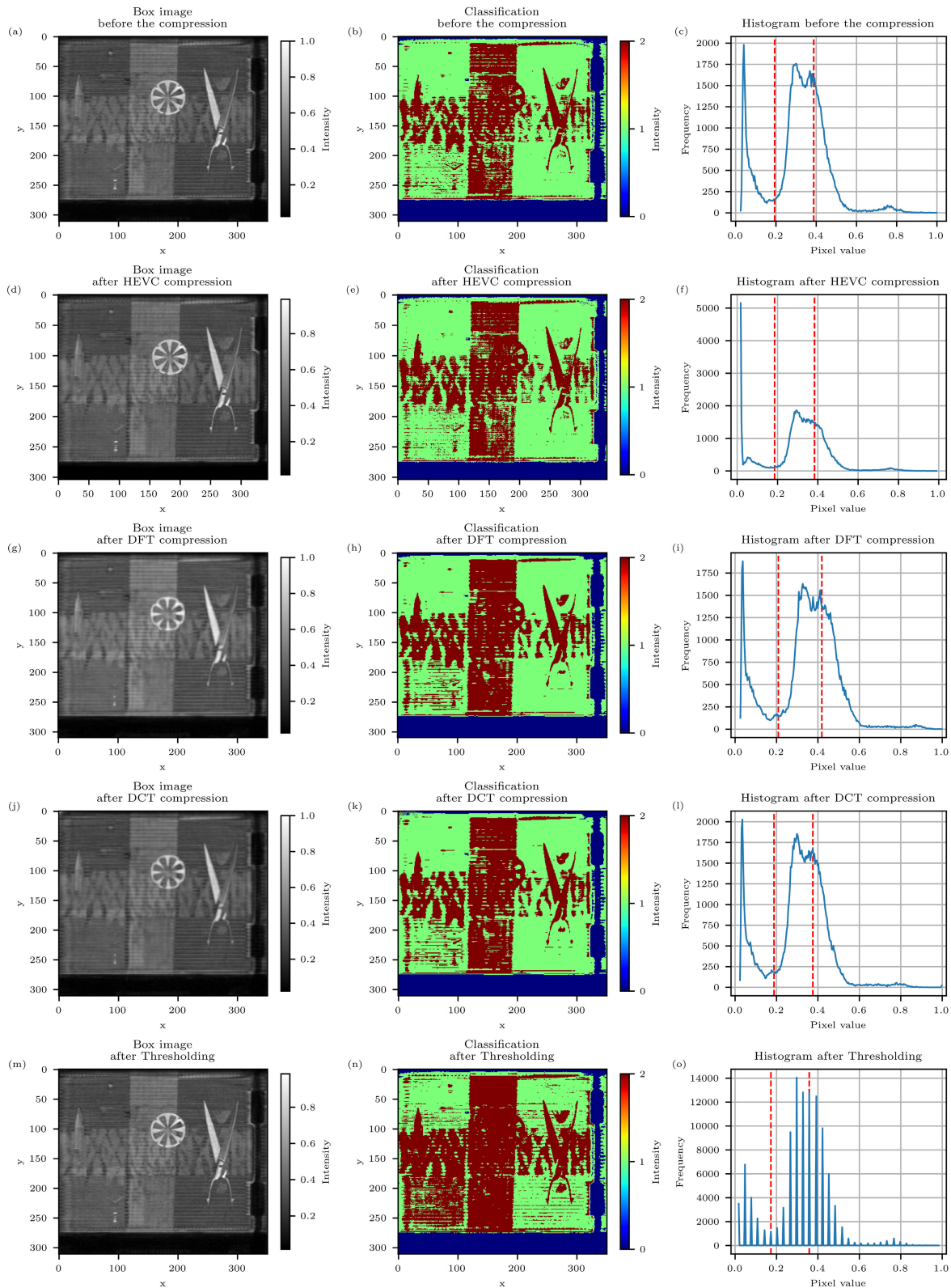
Fig. 13. Comparison of the box image compression using different algorithms. (a)–(c) Image before compression. (d)–(f) HEVC compression. (g)–(i) DFT compression. (j)–(l) DCT compression. (m)–(o) Thresholding compression. The left-hand column shows the grayscale images. The middle column shows the classification images with three classes based on Otsu's method. Values below the lower threshold are represented by blue, values above the higher threshold are represented by red, and values between both thresholds are represented by green. The right-hand column shows the corresponding histograms with Otsu thresholds indicated by the red lines.

As shown in Fig. 13(j)–(l), the DCT achieved a higher compression ratio of approximately 770 and a smaller data size of 109.3 kB. The corners of the objects were not displayed as sharply after compression. Moreover, the small openings in the Siemens star at the top and bottom were no longer visible in the grayscale image, and its center became larger. The classi-
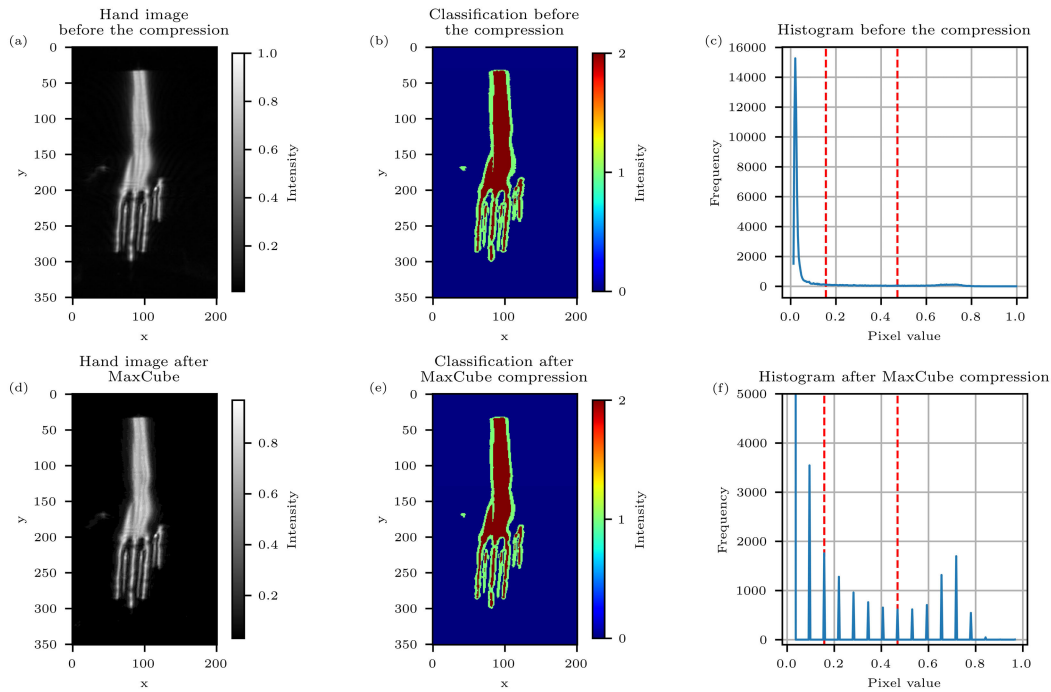
Fig. 14. Comparison of the hand images before and after MaxCube compression. (a)–(c) Initial situation before compression. (d)–(f) Results of MaxCube compression. The left-hand column shows the grayscale images. The middle column shows the classification images with three classes based on Otsu's method. The main parts that scattered a significant part of the radar waves back to the antennas in a normal direction are shown in red, whereas areas of the hand that reflected only part of the energy back to the antennas due to the surface's curvature are shown in green. Areas with hardly any reflection are shown in blue. The right-hand column shows the corresponding histograms with Otsu thresholds indicated by the red lines.

fication with Otsu's thresholds of 0.188 and 0.375 showed that the red values—that is, the values above the higher threshold—increased. The edge effects of the DCT resulted in values above 1, which were set to 1 by clipping. This can be seen in the histogram in Fig. 13(l), which shows a small increase in values of 1.

As shown in Fig. 13(m)–(o), Thresholding obtained a grayscale image with sharper edges than those obtained by the DFT and DCT. The compression ratio was 60, the data size was 1.394 MB, and Otsu's thresholds were 0.173 and 0.358. The classification resulted in even more red regions due to quantization and the fact that the difference between the original and compressed images increased, leading to a lower SSIM value. Furthermore, quantization achieved a sharper transition of the objects edges and an unchanged center of the Siemens star. The impact of quantization is clearly shown in Fig. 13(o). With the other algorithms and in the uncompressed image, zero values occurred most frequently. This was not the case with Thresholding because the threshold value was 0.0398 and thus lay slightly to the right of the first peak (compare with the histogram in Fig. 13(c)). Consequently, the smallest value in the histogram in Fig. 13(o), which occurred approximately 3500 times, was not the most frequent value.

B. Hand Radar Image Compression Results

Fig. 14(a)–(c) shows the hand image before compression. A comparison of the histogram in Fig. 14(c) with the box histogram in Fig. 13(c) shows that, due to the reflection of the radar waves on the skin surface, most pixel values were very small, and the interesting values accounted for only a small proportion. Nevertheless, Otsu's method also generated a classification here, with thresholds of 0.156 and 0.473.

The compression of the hand image using MaxCube is shown in Fig. 14(d)–(f). Despite a compression ratio of 1360 and a data size of 39.752 kB, no significant differences were observed in either the grayscale image or the classification image, with almost the same areas allocated to blue, green, and red. This was also reflected in the fairly close Otsu thresholds of 0.158 and 0.469. The effects of quantization can be seen in Fig. 14(f), where values close to zero appeared almost 57 000 times.

C. Comparison of the Algorithms

The individual compression ratios are summarized in Table III. HEVC achieved a good compression ratio of 120 and fine details and sharp edges were still visible in the image. The DFT achieved a higher compression ratio of 520 but resulted in the loss of fine details and an enlarged Siemens star center. The same was observed with DCT at a compression ratio of 770. Thresholding achieved a moderate compression ratio of 60 but preserved the sharp edges and a small Siemens star center, which were further improved by quantization.

Data compression was executed using an eight-core Intel® Core™ i7-9700 CPU at a 3 GHz clock frequency with 8 cores and 64 GB of RAM. HEVC compression lasted 183 s, DFT compression lasted 1.22 s, DCT compression lasted 0.93 s, Thresholding compression lasted 5.70 s, and MaxCube compression of the hand image lasted 0.071 s.

Table IV shows a comparison of the algorithms' compression results between the box and hand images. The algorithms

TABLE III

SUMMARY OF FIG. 13 AND FIG. 14 OF THE ACHIEVED RATIOS WITH THE DEPENDING VALUES FOR SSIM AND PSNR

Algorithm	Ratio	Rate savings	SSIM	PSNR
Uncompressed	1	0 %	1	∞
HEVC	120	99.17 %	0.895	37.4 dB
DFT	520	99.81 %	0.889	35.3 dB
DCT	770	99.87 %	0.895	36.6 dB
Thresholding	60	98.33 %	0.928	40.6 dB
MaxCube	1360	99.93 %	0.916[1]	38.8 dB[1]

[1] The values refer to the comparison of images *I* and *J* of the maximum projection.

TABLE IV

COMPARISON OF THE COMPRESSION ALGORITHMS BETWEEN THE BOX AND HAND IMAGE

Algorithm	Box		Hand	
	Ratio	SSIM	Ratio	SSIM
HEVC	120	0.895	920	0.883
DFT	520	0.897	190	0.973
DCT	770	0.895	280	0.978
Thresholding	60	0.928	420	0.933

used the same compression settings for both scenarios. The box SSIM was based on the 3D image, while the hand SSIM was based on the 2D maximum projection. HEVC and Thresholding achieved higher hand image than box image compression ratios with the same parameters, while the DFT and DCT achieved lower hand image compression ratios.

Since only one measurement object was depicted, most pixels belonged to the background and the areas between the individual layers of the image volume. Due to the large proportion of the background, which does not change suddenly between layers, HEVC achieved higher hand image than box image compression due to block formation.

The DFT and DCT obtained lower hand image compression ratios because in the background regions, in which only noise originally appeared, not all of the noise was removed. This resulted in more nonzero values, which prevented efficient compression using the LZMA. Optimizing the algorithm parameters described in Section V can increase the hand image compression ratio.

With Thresholding, only the values above the selected threshold are compressed, whereas those below the threshold are set to zero. Consequently, the number of zero values continues to increase, and more values can be represented by a short bit pattern using the LZMA. In contrast to the DFT and DCT, the smallest value obtained by Thresholding was also by far the most frequent when the hand image was compressed. Furthermore, a smaller quantization can be used with Thresholding than with DFT and DCT, which means that the number of different values is also reduced.

D. Discussion of the Results

Our evaluation results show that 3D radar images can be compressed using the state-of-the-art HEVC standard, with a good compression ratio. Moreover, although the DFT-based compression introduced in [13] was initially designed for automotive use, it can also be used in radar imaging with

no significant changes. Overall, all the algorithms presented here can achieve better compression ratios when compressing reconstructed radar images than raw data.

Our detailed evaluation results show that the DFT and DCT achieve better compression than HEVC in most cases, with DCT performing slightly better than DFT. Moreover, both the DFT and DCT are significantly faster than HEVC, with the DCT being faster than the DFT.

Thresholding is a simple compression variant, with all values below a certain threshold set to zero. In terms of compression duration, Thresholding is considerably faster than HEVC but slower than the DFT and DCT. Moreover, it achieves a lower compression ratio than HEVC, DFT, and DCT. However, unlike the DFT and DCT, it does not require an inverse transform during decompression.

MaxCube can achieve the highest compression ratio and the fastest compression. We specifically designed this compression algorithm for radar images of nontransparent objects.

We also examined a combination of Thresholding and MaxCube, in which Thresholding was also applied to the maximum intensity projection (Matrix 1 of MaxCube). However, the results were inferior to than those achieved by MaxCube alone and are therefore not reported here. Other combinations, such as DFT or DCT with MaxCube, are also conceivable but were not examined in this study.

VII. CONCLUSION

Our results show that the DFT shows better compression performance than HEVC, as evaluated using image processing metrics. This contrasts with the results obtained in [13], in which range–Doppler maps were compared. Moreover, our results show that our approaches—the DCT-based algorithm, Thresholding, and MaxCube—can achieve better results than HEVC and the DFT. However, in which cases the DCT, Thresholding, or MaxCube performs better depends on the comparison metric used and the desired compression ratio.

In this work, we considered only two scenarios: one with transparent objects (box contents) and one with a nontransparent object (hand), because it takes a lot of effort to generate different images. Nevertheless, we presume that comparable results can be achieved using similar images within the respective scenario. Further studies with several different measurement scenarios should be conducted. Since the phase is not required for many applications of radar imaging after the image reconstruction is done, the image volume compression in this work did not include the phase. Evaluating recent compression standards, such as Versatile Video Coding (VVC) or the Discrete Wavelet Transform, is also an option. Since the 3D shape of the data, compression using Tucker decomposition [35] is also conceivable. Finally, future studies could calculate the average rate savings at constant picture qualities using the Bjontegaard Delta metric [36].

REFERENCES

[1] S. S. Ahmed, "Microwave imaging in security—Two decades of innovation," *IEEE J. Microw.*, vol. 1, no. 1, pp. 191–201, Jan. 2021, doi: 10.1109/JMW.2020.3035790.

[2] I. Ullmann, J. Adametz, D. Oppelt, A. Benedikter, and M. Vossiek, "Non-destructive testing of arbitrarily shaped refractive objects with millimetre-wave synthetic aperture radar imaging," *J. Sensors Sensor Syst.*, vol. 7, no. 1, pp. 309–317, Apr. 2018, doi: 10.5194/jsss-7-309-2018.

[3] C. Waldschmidt, J. Hasch, and W. Menzel, "Automotive radar—From first efforts to future systems," *IEEE J. Microw.*, vol. 1, no. 1, pp. 135–148, Jan. 2021, doi: 10.1109/JMW.2020.3033616.

[4] The Consultative Committee for Space Data Systems, "Lossless data compression," Recommendation for Space Data System Standards, Washington, DC, USA, Tech. Rep. CCSDS 121.0-B-3, Aug. 2020.

[5] The Consultative Committee for Space Data Systems, "Image data compression," Recommendation for Space Data System Standards, Washington, DC, USA, Tech. Rep. CCSDS 122.0-B-2, Sep. 2017.

[6] The Consultative Committee for Space Data Systems, "Low-complexity lossless and near-lossless multispectral and hyperspectral image compression," Recommendation for Space Data System Standards, Washington, DC, USA, Tech. Rep. CCSDS 123.0-B-2, Feb. 2019.

[7] Z. Wang, Y. Xie, S. Song, W. Han, Z. Chen, and Y. Wu, "Data compression and transmission technology of USV radar image," in *Proc. IEEE Int. Conf. Unmanned Syst. (ICUS)*, Beijing, China, Oct. 2021, pp. 644–647, doi: 10.1109/ICUS52573.2021.9641397.

[8] S. Bhattacharya, T. Blumensath, B. Mulgrew, and M. Davies, "Synthetic aperture radar raw data encoding using compressed sensing," in *Proc. IEEE Radar Conf.*, Rome, Italy, May 2008, pp. 1–5, doi: 10.1109/RADAR.2008.4720896.

[9] A. Andreadis, G. Benelli, A. Garzelli, and S. Susini, "A DCT-based adaptive compression algorithm customized for radar imagery," in *Proc. IEEE Int. Geosci. Remote Sens. Symp. Remote Sens.-Sci. Vis. Sustain. Develop. (IGARSS)*, Singapore, vol. 4, Aug. 1997, pp. 1993–1995, doi: 10.1109/IGARSS.1997.609183.

[10] P. Eichel and R. W. Ives, "Compression of complex-valued SAR images," *IEEE Trans. Image Process.*, vol. 8, no. 10, pp. 1483–1487, Oct. 1999, doi: 10.1109/83.791978.

[11] L. Guangyue and S. Chao, "Novel scheme for inverse synthetic aperture radar (ISAR) imaging data compression," in *Proc. CIE Int. Conf. Radar*, Beijing, China, Oct. 2001, pp. 658–661, doi: 10.1109/ICR.2001.984803.

[12] K. Root, J. Adametz, F. Gumbmann, I. Ullmann, and M. Vossiek, "Improved threat detection in walk-through security scanning using an optimized polarimetric target decomposition method," *IEEE J. Microw.*, vol. 3, no. 1, pp. 16–28, Jan. 2023, doi: 10.1109/JMW.2022.3209164.

[13] G. Körner et al., "Applicability and performance of standard compression methods for efficient data transmission and storage in radar networks," *IEEE J. Microw.*, vol. 2, no. 1, pp. 78–96, Jan. 2022, doi: 10.1109/JMW.2021.3119781.

[14] X. Li, X. Wang, Q. Yang, and S. Fu, "Signal processing for TDM MIMO FMCW millimeter-wave radar sensors," *IEEE Access*, vol. 9, pp. 167959–167971, 2021, doi: 10.1109/ACCESS.2021.3137387.

[15] I. G. Cumming and F. H. Wong, *Digital Processing of Synthetic Aperture Radar Data: Algorithms and Implementation*. Norwood, MA, USA: Artech House, 2005.

[16] S. S. Ahmed, A. Schiessl, F. Gumbmann, M. Tiebout, S. Methfessel, and L.-P. Schmidt, "Advanced microwave imaging," *IEEE Microw. Mag.*, vol. 13, no. 6, pp. 26–43, Sep. 2012, doi: 10.1109/MMM.2012.2205772.

[17] I. Ullmann et al., "Circular polarization millimeter wave SAR imaging using 3D-printed helix antennas," *Proc. SPIE*, vol. 11541, Sep. 2020, Art. no. 1154108, doi: 10.1117/12.2573952.

[18] J. Bräunig et al., "An ultra-efficient approach for high-resolution MIMO radar imaging of human hand poses," *IEEE Trans. Radar Syst.*, vol. 1, pp. 468–480, Aug. 2023, doi: 10.1109/TRS.2023.3309574.

[19] F. Gumbmann and A. Schiessl, "Short-range imaging system with a nonuniform SFCW approach," *IEEE Trans. Microw. Theory Techn.*, vol. 65, no. 4, pp. 1345–1354, Apr. 2017, doi: 10.1109/TMTT.2017.2649501.

[20] J. Gazdag, "Wave equation migration with the phase-shift method," *Geophysics*, vol. 43, no. 7, pp. 1342–1351, Dec. 1978, doi: 10.1190/1.1440899.

[21] H. Zhang, W.-S. Benedix, D. Plettemeier, and V. Ciarletti, "Radar subsurface imaging by phase shift migration algorithm," in *Proc. Eur. Microw. Conf.*, Nuremberg, Germany, Oct. 2013, pp. 1843–1846.

[22] A. Horé and D. Ziou, "Image quality metrics: PSNR vs. SSIM," in *Proc. 20th Int. Conf. Pattern Recognit.*, Istanbul, Turkey, Aug. 2010, pp. 2366–2369, doi: 10.1109/ICPR.2010.579.

[23] N. M. Suaib, M. H. Marhaban, M. I. Saripan, and S. A. Ahmad, "Performance evaluation of feature detection and feature matching for stereo visual odometry using SIFT and SURF," in *Proc. IEEE REGION 10 Symp.*, Kuala Lumpur, Malaysia, Apr. 2014, pp. 200–203, doi: 10.1109/TENCONSPRING.2014.6863025.

[24] The Scikit-Image Team. (Jun. 23, 2023). *Image Processing in Python*. Scikit-Image. [Online]. Available: https://scikit-image.org/docs/stable/api/skimage.metrics.html#skimage.metrics.structural_similarity

[25] N. Otsu, "A threshold selection method from gray-level histograms," *IEEE Trans. Syst. Man, Cybern.*, vol. SMC-9, no. 1, pp. 62–66, Jan. 1979.

[26] X. Xiangyuang, X. Shengzhou, J. Lianghai, and E. Song, "Characteristic analysis of Otsu threshold and its applications," *Pattern Recognit. Lett.*, vol. 32, no. 7, pp. 956–961, May 2011, doi: 10.1016/j.patrec.2011.01.021.

[27] *High-Efficiency Video Coding*, Document ITU-T Rec. H.265 and ISO/IEC 23008-2. ITU-T and ISO/IEC JTC 1/SC 29/WG 11 (MPEG), Apr. 2013.

[28] GitLab. *Joint Collaborative Team on Video Coding (JCT-VC)*. Accessed: May 17, 2021. [Online]. Available: https://vcgit.hhi.fraunhofer.de/jvet/HM

[29] F. Bossen, *Common Test Conditions and Software Reference Configurations*, Document JCTVC-L1100, ITU-T VCEG and ISO/IEC MPEG (JCT-VC), Geneva, Switzerland, 2013.

[30] X. Zhao and B. Li, "Implementation of the LZMA compression algorithm on FPGA," in *Proc. Int. Conf. Electron Devices Solid-State Circuits (EDSSC)*, Taiwan, Oct. 2017, pp. 1–2, doi: 10.1109/EDSSC.2017.8126506.

[31] N. Ahmed, T. Natarajan, and K. R. Rao, "Discrete cosine transform," *IEEE Trans. Comput.*, vol. COM-100, no. 1, pp. 90–93, Jan. 1974, doi: 10.1109/T-C.1974.223784.

[32] M. Kronauge and H. Rohling, "Fast two-dimensional CFAR procedure," *IEEE Trans. Aerosp. Electron. Syst.*, vol. 49, no. 3, pp. 1817–1823, Jul. 2013, doi: 10.1109/TAES.2013.6558022.

[33] M. Rahimi and M. Yazdi, "A new hybrid algorithm for speckle noise reduction of SAR images based on mean-median filter and SRAD method," in *Proc. 2nd Int. Conf. Pattern Recognit. Image Anal. (IPRIA)*, Rasht, Iran, Mar. 2015, pp. 1–6, doi: 10.1109/PRIA.2015.7161623.

[34] C. Yeo, H. L. Tan, and Y. H. Tan, "On rate distortion optimization using SSIM," *IEEE Trans. Circuits Syst. Video Technol.*, vol. 23, no. 7, pp. 1170–1181, Jul. 2013, doi: 10.1109/TCSVT.2013.2240918.

[35] L. R. Tucker, "Some mathematical notes on three-mode factor analysis," *Psychometrika*, vol. 31, no. 3, pp. 279–311, Sep. 1966, doi: 10.1007/BF02289464.

[36] G. Bjøntegaard, *Calculation of Average PSNR Differences Between RD Curves*, Document VCEG-M33, Austin, TX, USA, Apr. 2001.

Rainer Rückert received the B.Eng. degree in electrical engineering and information technology and the M.Eng. degree in electronic and mechatronic systems from Technische Hochschule Nürnberg Georg Simon Ohm, Nuremberg, Germany, in 2017 and 2019, respectively.

From 2015 to 2018, he worked in the field of automotive control systems with Continental AG, as part of his cooperative education. In 2018, he joined the Institute of Microwaves and Photonics (LHFT), Friedrich-Alexander-Universität Erlangen-Nürnberg (FAU), Erlangen, Germany. His research focuses on radar signal processing and radar hardware.
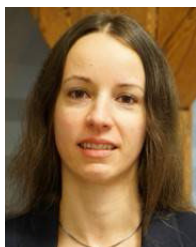
Ingrid Ullmann (Member, IEEE) received the M.Sc. and Ph.D. degrees in electrical engineering from Friedrich-Alexander-Universität Erlangen-Nürnberg (FAU), Erlangen, Germany, in 2016 and 2021, respectively.

She is currently a Post-Doctoral Researcher and the Head of the Research Group "Wave-Based Imaging Techniques," Institute of Microwaves and Photonics, FAU. In 2022, she spent one month as a Visiting Researcher with the Microwave Sensing, Signals and Systems Group, Delft University of Technology, Delft, The Netherlands. Her research interests include radar imaging and radar signal processing for nondestructive testing, security screening, and medical and automotive applications.

Dr. Ullmann received the Argus Science Award (sponsored by Airbus Defense and Space, currently Hensoldt) in 2016 and the EuRAD Conference Prize in 2019. She serves as a reviewer for the European Radar Conference (EuRAD) and various journals in the field of microwaves. Since 2022, she has been an Associate Editor of IEEE TRANSACTIONS ON RADAR SYSTEMS.

he was the Head of the Department of Electrical Engineering and the Vice Dean of the Faculty of Engineering, FAU. He has authored over 450 journals and conference papers and has more than 120 patents granted or pending. His research interests include image and video signal processing and coding and multimedia communication.

He is a member of the IEEE Image, Video, and Multidimensional Signal Processing Technical Committee; the Scientific Advisory Board of the German VDE/ITG; the Bavarian Academy of Sciences; and the European Academy of Sciences and Arts. He was a Siemens Inventor of the Year 1998 and received the 1999 ITG Award. He received several IEEE Best Paper Awards, including the Paul Dan Cristea Special Award in 2013 and his group won the Grand Video Compression Challenge from the Picture Coding Symposium 2013. The Faculty of Engineering with FAU and the State of Bavaria honored him with Teaching Awards, in 2015 and 2020, respectively. He served as an Associate Editor for IEEE TRANSACTIONS ON CIRCUITS AND SYSTEMS FOR VIDEO TECHNOLOGY. He was a Guest Editor of the IEEE JOURNAL OF SELECTED TOPICS IN SIGNAL PROCESSING. He is a member of the Editorial Board of *IEEE Circuits and Systems Magazine*.

Christian Herglotz (Member, IEEE) received the Dipl.-Ing. degree in electrical engineering and information technology and the Dipl.-Wirt.-Ing. degree in business administration and economics from Rheinisch-Westfälische Technische Hochschule (RWTH) Aachen University, Germany, in 2011 and 2012, respectively, and the Dr.-Ing. degree from Friedrich-Alexander Universität Erlangen-Nürnberg (FAU), Germany, in 2017.

From 2012 to 2023, he was a Research Scientist with the Chair of Multimedia Communications and Signal Processing, FAU. From 2018 to 2019, he was a Post-Doctoral Fellow with École de Technologie Supérieure, in collaboration with Summit Tech Multimedia, Montréal, Canada, on energy efficient VR technologies. Since 2023, he has been a Substitute Professor of computer engineering with Brandenburgische Technische Universität Cottbus-Senftenberg, Germany. His current research interests include energy efficient video communications, video coding, and efficient hardware and software implementations for image and video processing. Since 2020, he has been with the Visual Signal Processing and Communications Technical Committee, IEEE Circuits and Systems Society. Since 2023, he has been serving as an Associate Editor for IEEE TRANSACTIONS ON CIRCUITS AND SYSTEMS FOR VIDEO TECHNOLOGY.

Martin Vossiek (Fellow, IEEE) received the Ph.D. degree from Ruhr-Universität Bochum, Bochum, Germany, in 1996.

In 1996, he joined Siemens Corporate Technology, Munich, Germany, where he was the Head of the Microwave Systems Group, from 2000 to 2003. Since 2003, he has been a Full Professor with Clausthal University, Clausthal-Zellerfeld, Germany. Since 2011, he has been the Chair of the Institute of Microwaves and Photonics (LHFT), Friedrich-Alexander-Universität Erlangen-Nürnberg (FAU), Erlangen, Germany. Since 2021, he has also been the Spokesperson for the DFG Collaborative Research Center 1483 EmkinS. He has authored or coauthored more than 350 articles. His research has led to more than 100 granted patents. His current research interests include radar, microwave systems, wave-based imaging, transponders, RF identification, communication, wireless sensors, and locating systems.

Dr. Vossiek is a member of the German National Academy of Science and Engineering (acatech) and the German Research Foundation (DFG) Review Board. He is also a member of the IEEE Microwave Theory and Technology (MTT) Technical Committees for MTT-24 Microwave/mm-wave Radar, Sensing, and Array Systems; MTT-27 Connected and Autonomous Systems (as the founding Chair); and MTT-29 Microwave Aerospace Systems. He has received numerous best paper prizes and other awards. In 2019, he received the Microwave Application Award by the IEEE MTT Society (MTT-S) for Pioneering Research in Wireless Local Positioning Systems. He also serves on the Advisory Board of the IEEE CRFID Technical Committee on Motion Capture and Localization. He has been a member of organizing committees and technical program committees of many international conferences and has served on the review boards for numerous technical journals. From 2013 to 2019, he was an Associate Editor of IEEE TRANSACTIONS ON MICROWAVE THEORY AND TECHNIQUES. Since October 2022, he has been the Associate Editor-in-Chief of IEEE TRANSACTIONS ON RADAR SYSTEM.

André Kaup (Fellow, IEEE) received the Dipl.-Ing. and Dr.-Ing. degrees in electrical engineering from RWTH Aachen University, Aachen, Germany, in 1989 and 1995, respectively. He joined Siemens Corporate Technology, Munich, Germany, in 1995, and became the Head of the Mobile Applications and Services Group in 1999. Since 2001, he has been a Full Professor and the Head of the Chair of Multimedia Communications and Signal Processing, Friedrich-Alexander Universität Erlangen-Nürnberg (FAU), Germany. From 2005 to 2007, he was a Vice Speaker of the DFG Collaborative Research Center 603. From 2015 to 2017,